EUROPEAN ORGANIZATION FOR NUCLEAR RESEARCH

CERN/DRDC 94-12
RD-34 status report
March 1, 1994

RD-34 STATUS REPORT

Developments for a Scintillator Tile Sampling Hadron Calorimeter with " Longitudinal" Tile Configuration

F. Ariztizabal, M. Bosman, M. Cavalli-Sforza, E. Efthymiopoulos, C. Padilla, F. Teubert
IFAE, Universitat Autonoma de Barcelona, Spain

R. Arsenescu, C. Blag, V. Boldea, S. Dita
Institute for Atomic Physics, Bucharest, Rumania

Z. Ajaltouni, F. Badaud, N. Bouhemaid, P. Brette, M. Brossard, R. Chadelas, J.-C. Chevaleyre, M. Crouau, F. Daudon, J.-J. Dugne, B. Michel, G. Montarou, G.S. Muanza, D. Pallin, L.-P. Says, F. Vazeille
LPC, Clermont-Ferrand, France

O. Gildemeister, A. Henriques, J. Ivarsson, M. Nessi, L. Poggioli, P. Sonderegger
CERN, Geneva, Switzerland

H. Hakopian
Erevan Physics Institute, Armenia

A. Amorim, M. David, P. Ferreira, A. Gomes, A. Maio, L. Peralta
LIP and University of Lisbon, Lisbon, Portugal

R. Leitner, M. Suk, P. Tas
University of Prague, Czechoslovakia

L. Caloba, M. Gaspar, F. Marroquin, A. Pereira, J.M. Seixas, Z. Thome
COPPE/EE/UFRJ, Rio de Janeiro, Brazil

M. Kostrikov, M. Kulagin, V. Lapin, Y. Protopopov, A. Solodkov, A. Zaitsev
IHEP, Protvino, Russia

*Spokespersons: M. Cavalli-Sforza/M. Nessi

Abstract

The first prototype of a scintillator tile hadron calorimeter with longitudinal tile orientation and wavelength shifting fiber readout has been built and tested with pion, electron and muon beams at the CERN SPS. This innovative geometry combines good performance and a simple and cost effective assembly procedure. Calibration and monitoring of this detector have also been investigated. Some results on radiation hardeness are given as an appendix.

Contents

1 Introduction

The use of scintillator tiles as active material in sampling calorimetry has a number of attractive features in terms of speed, easy read out and low noise level. In all calorimeters of this type costructed up to now, the tiles are placed normal to the particles trajectories, which makes it nontrivial to read out the light while maintaining detector hermeticity.

The case for the hadron calorimeter concept investigated here is based on measuring hadron energies after the particles have traversed a thick (about $2\Lambda_{int}$) electromagnetic (EM) compartment. Specific Monte Carlo simulations indicate that in a hadron calorimeter placed in such an environment the orientation of the scintillator tiles with respect to the direction of the primary particles does not affect the energy resolution for hadrons or jets, provided that the tiles are staggered in depth in order to assure a good sampling homogeneity and that the path of a track segment in the scintillator material is not too long (Ref. [1]). Recently, other calorimeter concepts, such as the "spaghetti" calorimeter [2] and the liquid argon accordion calorimeter [3] have demonstrated similarly effective ways of longitudinally sampling the shower development.

The development of this new design concept is the purpose of a recently started LHC R&D activity [4].

Starting from a barrel calorimeter divided in sectors that span a given azimuthal interval $\Delta\phi$, the basic geometric concept is to orient the scintillator tiles in the $r-\phi$ plane. The tiles traverse the width of a sector module (see Figure 1). Wavelength shifting (WLS) fibers running straight in the radial direction read out the scintillator tiles at both of their free radial edges and are thus accessible from the side faces of each module. Fibers from different tiles are grouped and read out together, thus defining the read out cells; in this manner both axial (along z) and longitudinal (along r) segmentation are obtained, which can be chosen to define a pseudo–pointing geometry for non zero rapidity.

The mechanical structure consists of a stack of a large number of trapezoidal steel plates of only a few shapes, which periodically repeat along the z direction. This simplifies both the construction of the iron tiles and the assembly procedure.

In order to check this concept, three calorimeter modules were built and exposed to high energy pion, electron and muon beams at the CERN Super Proton Synchrotron (SPS) in a standalone mode, *i.e.* without EM section in front. Results on energy resolution, linearity and uniformity of response are presented, as well as calibration results.

This paper is organized as follows: Section 2 describes in some detail the components of the prototype and its construction. The monitoring and intercalibration systems are presented in Section 3 and the setup on the test beam, the data taking and data selection procedures in Section 4. The beam test results are discussed in Section 5. Finally Section 6 draws the conclusions and outlines some future prospects.

2 The Prototype Calorimeter

2.1 Mechanical construction

The prototype calorimeter is composed of three sector modules, each spanning $2\pi/64$ in azimuth, 100 cm in the axial (z) direction, and 180 cm in the radial direction (from an inner radius of 200 cm to an outer radius of 380 cm, in colliding beams geometry). The radial dimension amounts to about 9 interaction lengths.

The iron structure of each test module consists of 57 repeated "periods" sandwiched between two iron end plates of 20 mm thickness (see Fig. 2). Each period consists of 4 layers. The first and third layer are formed by large trapezoidal steel plates, 5mm thick, spanning the full radial dimension of the module (master plates, 180 cm long). The second and fourth layer of each period consist of a series of nine small trapezoidal steel plates, 4 mm thick, of 10 cm radial dimension and different widths according to their radial position (spacer plates). Along the radial direction, 10 cm gaps are left between spacer plates of the same layer for the later introduction of the scintillators. The spacer plates are staggered in radius between layers 2 and 4.

Each spacer plate has two 8 mm diameter holes on the (radial) axis of the trapezoid, spaced by 70 mm. Corresponding holes are provided in the master plates. All iron plates have been laser cut to a precision of ± 0.05 mm, including the positions of the holes [1]. The dimensional tolerance on the thickness of the laminated iron plates has been specified at ± 0.05 mm; this tolerance was met without difficulties.

Each module was piled up vertically, against a reference plane. In stacking the successive layers of the module the spacer plates were placed by means of spring pins pressed into the 8mm holes, joining a spacer plate to the 2 adjacent master plates. The mounted spring pins leave continuous longitudinal channels of 6.5 mm diameter, through which 6 mm rods are fed once the stack is completed. These series of rods serve to apply a distributed pressure to the stack. On the outer face of the compressed stack (at large radius) a strong steel profile is welded, to give rigidity to the structure and at the same time support the light detectors.

Every second rod has an axial hole with an internal diameter of 2 mm. A radioactive ^{137}Cs source can be inserted into the holes for calibration purposes, allowing consecutive excitation of each scintillator tile.

All mechanical operations have been achieved easily, thus demonstrating the time and cost effectiveness of this concept, in the perspective of the construction of a large hadron detector for the ATLAS experiment at LHC. The planarity of each ϕ face of the modules has been measured to be better than 0.2 mm over the whole surface. The module structure displays good rigidity, allowing crane

[1] For the case of the construction of a large calorimeter for LHC, punching of the plates has been envisaged as a more economic procedure

manipulation without apparent deformations. The weight of a sector module is approximately 3.5 tons.

During installation the three sectors have been linked to each other and positioned on a scanning table for the beam tests. The three sectors mounted side by side have an entrance face of 0.6×1 m^2. The iron to scintillator ratio is 4.67 to 1 in volume.

2.2 The scintillators and the WLS fiber system

The scintillator tiles are produced by an injection molding procedure developed at IHEP Protvino; the base is of polystyrene, to which primary and secondary wave-length shifting (WLS) dopants (PTP, 1.5% and POPOP, 0.3%) are added. The dopants and their concentrations have been chosen to optimize the light yield and the efficiency of the light coupling to the fiber.

The injection molding procedure is both efficient and economical: only 2 minutes/tile are required to produce the finished tiles, with grooves for fiber insertion, chamfered edges (as described below) and holes for the traversing rods. No additional machining or polishing steps are required. The tiles are 3 mm thick; the precisions obtained are $(+0, -0.15)$ mm on all lateral dimensions.

The coupling of the tiles to the fibers is shown in Figure 2. Two fibers are air-coupled to each tile by placing them in 1.1 mm grooves of square section at the radial edges of the tile. The adjacent edges are chamfered at 45^0. The scintillator tiles are wrapped in white paper and the readout edges are covered with an aluminized mylar reflector.

Commercially available fibers (Bicron BCF91A) have been used to read out the scintillation light. These fibers absorb the blue light from the tiles and re-emit in the green (peaking at about 480 nm). The fibers emission has a decay time of about 10 ns; the light attenuation length is about 2 m. The uniformity of the response has been improved by sputtering an Aluminum layer at the fiber end, obtaining a reflectivity of about 85%.

Scintillating tiles were inserted into the modules after completing the steel mechanical assembly, by temporarily removing the compression rods. Finally, the fibers were slid into the scintillator grooves.

2.3 The readout system

At the read-out end the fibers of each read-out cell are grouped, glued, diamond-polished and air–coupled to a solid PMMA light mixer, which in turn is air–coupled to a PM tube as the light detector. The latter air gaps measure 1 mm. The optimized shape of the mixers is a parallelepiped of $9 \times 9 \times 14$ mm^3.

The prototype calorimeter is longitudinally divided into 4 sections. As mentioned in the Introduction, this was obtained by reading longitudinal groups of tiles by means of different fibers (proceeding inwards in radius: tiles 1 to 6 in

section 4, 7 to 11 in section 3, 12 to 15 in section 2 and 16 to 18 in section 1). The width of the read-out cells in the z direction is about 20 cm (the 57 periods are divided into 5 cells of 12, 11, 11, 11 and 12 periods each). Each module therefore contains 5×4 cells, each independently read out from both sides, leading to a total of 40 light detectors per module. For the test modules relatively large photomultipliers (XP2012 5/4" blue) were used, because they could be recovered from a previous experiment.

To increase the dynamic range of the read-out, the anode signal from each PMT is fed into an active splitter, one output of which is sent unchanged into a 12-bit charge ADC, the other output is amplified by a factor ~ 10 before being fed into an ADC. The gain of the PMTs was set to deliver ~ 6 pC/GeV. The ADC gain is 4 counts/pC. The data discussed in this paper were taken with an ADC gate width of 350 ns. Sparse data readout was implemented: signals smaller than 4 counts above the pedestal value were not recorded. This corresponds to a cutoff of 17 MeV in the amplified channels.

3 Monitoring and intercalibration

The tile calorimeter design concept incorporates, as already pointed out, the option of running a radioactive source through each scintillating tile; the current induced in the PMT is proportional to the gain of the PMT and to the photoelectron yield of the calorimeter for the scintillation light induced by the source. Such a system was implemented for the prototype calorimeter; it was used when setting the HV of each PMT, to obtain uniform response of each readout cell. More generally such a system allows to control the spacial uniformity of the calorimeter's response and to monitor any changes in time if they occur.

Separate measurements of the PMT gains are necessary in order to monitor the response of the calorimeter to particles independently of gain drift. A pulsed laser system, illuminating each PMT by means of clear fibers, has been built and operated for this purpose; it also provides measurements of the linearity of the photomultipliers, and, after determining the energy/charge conversion constant of the calorimeter by response to particle beams, to determine the photoelectron yield.

Finally, the overall conversion gain of splitters and ADCs was intercalibrated by means of a charge-injection system. The operation and results obtained with the source and laser systems are described next.

3.1 The movable source system

A 5 mCi ^{137}Cs source, 5mm long, is embedded into a thin stainless steel tube (outer diameter of 1.3 mm) which can be inserted into the hollow rods along the z direction. The source tube is moved by a computer-controlled DC motor;

the position is measured by an encoder. The PMT current is measured with a pAmeter. In operation, the source is pushed all the way to the end of the hollow rod, and then retracted in 2 mm steps; at each step, currents of all 10 PMTs viewing the scintillators along the source path are read out. For the nominal gain of 2×10^6, the source-induced current is about 300 nA and the dark current is 1 to 5 nA.

Figure 3 shows a current measurement along the full z dimension of the calorimeter. Five excitation curves, corresponding to the 5 readout cells along the 1 m path, are superposed. Within each curve, a multiple peak/valley structure is evident; the local peaks correspond to the passage of the source across each individual scintillator tile. This is due to the fact that the mean path in Iron of the ^{137}Cs 0.66 MeV photons is close to the periodicity in z of the scintillator-Iron stack. This feature is very useful to control the quality of the detector after assembly. In the example shown in Figure 3, one observes a suppressed peak in the second cell which is due to a bad fiber–tile coupling (only a handful of such cases were observed out of $\sim$ 3000 tiles in the prototype).

For each PMT (2 PMTs/cell) an intercalibration constant is calculated, by integrating the current distribution shown in Figure 3 and then subtracting the dark current contribution. This result is then divided by the FWHM of the distribution to correct for the fact that the outer cells contain 12 tiles and the inner cells 11 tiles. The final constants are then calculated by averaging the values measured for the different tiles belonging to that cell.

The calorimeter intercalibration procedure consists of three steps. First, a measurement of the response of each cell is made by the procedure described above. Second, the voltage of each PMT is set to a value which gives the same current for each cell, based on the results of the first step, but using only one central point in each cell. The *r.m.s.* deviation from the mean of this precalibration of the cells was found to be 3.5 %. Finally the gains are measured again with full scans through all tiles of a cell. This provides the data for calculating the final intercalibration constants which are then used for the offline analysis of the test beam data. The stability of the constants measured 4 times over a period of 3 weeks (spanning a test beam run) was 1.2 %, without correcting for PMT gain drift.

The reproducibility of the source intercalibration was measured with the following method: the ratio of the calibrations constants from two rows of tiles viewed by the same PMT is formed. In this ratio the gain of the phototube cancels; however this ratio is in general not 1 because of tile-to-tile differences in light yield, coupling to fibers, fiber-to fiber differences, etc. This same ratio is measured at another time. Forming the ratio of the two ratios, the tile and fiber fluctuations cancel out; the remaining dispersion in the ratio-of-ratios is due to the error in the individual measurements. Figure 4 shows the distribution of the double ratios: the sigma of the distribution is 1.8% which corresponds to a precision for an individual calibration constant of $1.8\%/\sqrt{4} = 0.9\%$.

Statistical information about the tile-to-tile and fiber-to-fiber differences has also been extracted form the large databases accumulated for intercalibration stability studies. The variation of the individual-tile peaks in the current scans gives a combined tile-plus-fiber response variation with $r.m.s. = 8\%$, wherein the tile-to-tile variation contributes with $r.m.s. = 5\%$; from this, the fiber-to fiber variation can be calculated, by subtracting in quadrature, giving $r.m.s. = 7\%$. The latter number includes the variation in response due to the difference in length of the fibers from different tiles. These results confirm laboratory measurements of the variation of the response of tiles and fibers, made before prototype construction.

3.2 The laser system

The core of this system is a frequency-doubled YLF 7300 laser (Spectra Physics); the laser is triggerable, and the intensity of each light pulse can be externally modulated; the system is fully computer controlled. The light ($\lambda = 523$ nm) is split between a timing PMT, two photodiodes whose averaged signals are used to monitor the laser intensity, and three secondary splitters, one for each prototype module. Each secondary splitter distributes light to the 40 PMTs of each module by means of clear fibers. During each beam spill, the laser is electronically driven to produce trains of light pulses; within each train, four pulses of increasing intensity span the PMT dynamic range.

The variation of the photomultiplier responses relative to the laser intensity, monitored on a pulse-to-pulse basis, allow to follow the time drift of the photomultiplier gains. A precision of 1% has been achieved; this can be further improved by accurately monitoring, in turn, the monitor photodiode response by means of a radioactive source.

The relative precision achieved in monitoring the laser intensity is shown in Figure 5, wherein the response of the two monitor photodiodes is shown. The response of a photomultiplier to 4 different pulse intensities is shown in Figure 6, as a function of the photodiode-monitored intensity of each light pulse. The dispersion in response along the vertical axis is due to photoelectron statistics (according to $r.m.s./\text{signal} = 1/\sqrt{N_{pe}}$); from this the gain of the photomultiplier and the photoelectron yield can be obtained. A typical number for the photoelectron yield is 21 ± 2 photoelectron/GeV, in agreement with measurements with electrons described further.

4 Experimental set-up

4.1 Beam line

Measurements were performed in the H2 beam line of the SPS at CERN. The calorimeter was mounted on a platform that moves horizontally, perpendicular to the beam line, with a precision of about 1 mm (z direction). The detector can also be rotated on its vertical axis, allowing to change the particle incidence angle θ to the plane defined by the tiles. Finally, the detector can be rotated around a horizontal axis, 200 cm upstream of the front face and parallel to it (corresponding to the colliding beam axis z) thereby reproducing any azimuthal (ϕ) incidence angle. The set up is shown in Fig. 7.

Upstream of the calorimeter, a trigger counter telescope was installed. It consists of 5 scintillation counters (S1 - S5), defining a beam spot of 2 cm diameter. Two delay-line wire chambers with x, y readout (BC1, BC2), 5 m from each other, have a resolution in x, y of about 300 μm.

4.2 Data taking and event selection

Data were taken with electron beams of 20, 40, 80 and 150 GeV, pion beams of 20, 40, 80, 150, 200 and 300 GeV and muons of 225 GeV at various θ and ϕ angles of incidence. The beam rates were $10^2 - 10^3$ particles over 2.6 s long spills. Beams were generally clean, with the longitudinally segmented calorimeter aiding in removing pion or electron contaminations, typically not exceeding the 1% level. Muons were easily removed by checking on the total energy deposited in the calorimeter. Single–track events were selected offline, by requiring the pulse heights of the counters S1 and S2 to be below 1.7 times the m.i.p. value. Particles at anomalous angles were removed by requiring that the x and y coordinates measured in the two beam chambers agree within 1 cm; beam halo was removed by cuts on x and y in the beam chambers.
The ADC signals were mutually intercalibrated making use of the Cs source calibration constants. No further correction was applied to the raw data.

5 Test Beam Results

5.1 Photoelectron yield

In a sampling calorimeter, care must be taken that the photoelectron yield is high enough that the energy resolution is not limited by photoelectron statistics. The resolution of such a calorimeter can be expressed by [6] :

$$\frac{\sigma}{E} = \frac{\sqrt{\sigma^2_{samp} + \sigma^2_{p.e.}}}{E} + c$$

where σ_{samp} describes the sampling fluctuations and $\sigma_{p.e.}$ the fluctuations due to photoelectron statistics. The contribution of the latter term can be directly determined by measuring the effect of a reduction of the light yield, obtained by means of neutral filters, on the total energy resolution σ/E. The measurements were done using the lowest-energy electrons available (20 GeV), in order to minimize the contribution to the resolution of the energy–independent term c. The calorimeter was rotated to 90^0 to the beam line, to take advantage of the relatively fine granularity of the calorimeter (3 mm scintillator followed by 14 mm of Iron) for particles impinging at this angle. An energy scan with 20, 40, 80 and 150 GeV electrons allowed to measure the energy-independent term $c = 0.4\%$. Since the number of photoelectrons, $N_{p.e.}$, is equal to $(\sigma_{p.e.}/E)^{-2}$, the formula above can be rewritten as

$$(\frac{\sigma}{E} - c)^2 \;=\; (\frac{\sigma_{samp}}{E})^2 \;+\; \frac{1}{fN_{p.e.}}$$

where f is the fraction of light passing the filter.

Figure 8. shows the quantity $(\sigma/E - c)^2$, with $c = 0.4\%$, as a function of the inverse of the average electron signal E, for 2 different tile sizes. As expected, a linear relationship is observed, from which the number of photoelectrons was determined. The mean number of photoelectrons produced per GeV shower energy (without filters, $f = 1$) is 20 ± 1 for tile 13, and 25 ± 1 for tile 9 (see tile numbering in section 2.3). The measured photoelectron yield, taking the smaller tile as representative for a typical shower, translates into a contribution to the calorimeter resolution of $\sigma_{p.e.} = 0.20$. The difference in photoelectron yield between the two tile sizes confirms previous laboratory measurements indicating that smaller tiles give more light.

5.2 Muons

An alternative cell intercalibration technique was explored by exposing the prototype calorimeter to muons impinging at 90^0 in the geometrical center of each of the 18 tiles.

About 15000 muons with $E = 225\ GeV$ were accumulated for each tile, to obtain precise fits to the peak of the energy loss distributions. A typical signal distribution, from a readout cell comprising 11 scintillator tiles, is shown in Figure 9. The peak is found by fitting to the distributions a Moyal function (Ref. [5]). This parametrization gives a reasonable representation of the peak region, while it does not account for the high-energy tail. The latter is probably due to the electromagnetic showers from higher-order QED processes, like bremsstrahlung or direct e^+e^- pair production, which are important in this energy range.

The correlation of the fitted muon peak values for each photomultiplier with the corresponding source calibration constant gives an *r.m.s.* spread of 6%. This spread represents the combined effect of the source and muon calibration errors;

it is believed to be dominated by the error on the position of the muon peak because the small dynamic range of muon signal (typically 24 ADC channels above pedestal, for the amplified signals) makes the peak value relatively sensitive to small pedestal shifts. An electronic readout chain with a better match to the calorimeter's dinamic range will improve the correlation of the muon and source intercalibration constants.

The response to muons incident at small θ angles is shown in Figure 10. Here the distributions show the signal in the entire calorimeter; the small signal increase seen at 20^0 is mostly a geometrical effect. The data in the first plot in the Figure 10 are for muons at 0.3^0 from the axis; this small deviation from incidence parallel to the tile plane ($\theta = 0^0$) is sufficient to avoid a significant change in sampling fraction.

The peaks in Figure 10 correspond to an energy deposition in the calorimeter of about 2.8 GeV, which can be compared to the expected energy deposition per bunch crossing at LHC nominal luminosity ($1.7 \times 10^{34}\ cm^{-2}sec^{-1}$) of 0.4 GeV into a $\Delta\eta \times \Delta\phi = 0.1 \times 0.1$ calorimeter cell. This gives a confortable margin for detecting isolated muons in the calorimeter at the LHC.

5.3 Electrons

When electrons directly impinge on this type of calorimeter, at small angles to the tile plane, the response is expected to be strongly position–dependent, *i.e.* to display the effect of the calorimeter periodicity along the z direction. This is because the calorimeter longitudinal segmentation (10 cm) for particles at small angle is much larger than the radiation length in Iron; therefore the response to electrons at small angles will depend on whether the initial impact point is in Iron or in the scintillator. Of course, this effect is of no consequence in the LHC environment, for which this calorimeter has been proposed, because it is to be preceded by an electromagnetic calorimeter that will fully absorb the electromagnetic showers.

An example of the position dependance of the electron signal is shown in Figure 11, where the electron impact point on the calorimeter front face is calculated using the information from the beam chambers, and the electron response is the mean of the signal in the calorimeter in each 1 mm bin. The data for Figure 11 were taken in three runs with electrons at 10^0, moving the calorimeter by 20 mm along z between runs. The 18 mm tile/iron periodicity is clearly visible.

Similar data were taken with electrons at 20, 40, 80 and 150 GeV, at incidence angles of $0^0, 10^0$ and 20^0, to obtain the electron response of the calorimeter. The response is calculated as the mean over one 18 mm period. It is seen to be linear versus energy at the 1% level for $\theta = 10^0, 20^0$, while at 0^0 there is a signal loss of a few percent at 20 and 40 GeV.

5.4 Pions

5.4.1 Uniformity of response

As for electrons, data were taken at several points along the calorimeter face, with pion incidence angles of $0^0, 10^0$ and 20^0, in order to check the uniformity of the calorimeter response.

The effect of tile periodicity is only observed at 0^0, as shown in Figure 12. Here the mean signal is plotted as a function of coordinate of impact on the calorimeter face, as for electrons. A structure with a 9 mm period can be seen, precisely reproducing the staggered tile/Iron geometry described in Section 2. No such structure is perceivable in position scans at 10^0 and 20^0. The non-uniformity seen at 0^0 will of course be substantially attenuated when hadrons reach this calorimeter after traversing a thick electromagnetic compartment.

More extensive response uniformity studies were performed with pions of 40 GeV and 80 GeV, at an angle of incidence of 10^0. A span of 60 cm on the front calorimeter face was explored with 80 GeV pions, moving the calorimeter by 3 cm in the z direction for each data point. The points at 80 GeV in Figure 13 are obtained by fitting the energy spectrum at each position to a Gaussian; the values for $8 \leq z \leq 20$ cm have been corrected for lateral leakage out of the positive z side of the calorimeter. These corrections were estimated by using the transverse and longitudinal energy distributions in the calorimeter obtained from the same set of data; the largest correction is +2.2%, at $z = 20$ cm. The signals are normalized to their mean; the distribution has an *r.m.s.* value of 0.9%, as shown in the insert.

A similar uniformity scan (performed with 40 GeV pions, about two months earlier) is also shown in Figure 13; it is clear that the small residual nonuniformities over the common data range are well correlated. This suggests that nonuniformities are due to actual physical features of the calorimeter, such as local differences in tile or fiber response.

5.4.2 Pion energy resolution

The energy resolution of the prototype calorimeter for pions has been studied by taking data over the full available energy range, 20 to 300 GeV, and at incidence angles of 0^0, 10^0 and 20^0. The observed energy spectra at 20^0 are shown in Figure 14. These spectra are directly obtained from the raw data; the only selection procedure applied is that described in Section 4, to better define the beam spot and the incident particle directions. The spectra are quite symmetric at all energies, and display small or no tails at high energy. Above 150 GeV some low energy tails appear, due longitudinal leakage of the hadronic shower in this test beam configuration, without an upstream EM compartment.

Peak and σ values were obtained from these energy spectra by gaussian fits over a $\pm 2\sigma$ range. The resulting σ/E resolutions are plotted in Figure 15 versus

$1/\sqrt{E}$; they are found to be well fit by a form

$$\frac{\sigma}{E} = \frac{A}{\sqrt{E}} + B$$

wherein the constant term B is directly added to the statistical term. It can be seen that the resolutions measured at 10^0 and 20^0 are described by the same statistical term (within errors) and similar constant terms. The resolutions at 0^0 have a different behaviour; the energy dependence is affected by a larger constant term, due to the nonuniformity of response at 0^0 shown above.

The values of both statistical and constant terms resolutions compare favourably with results obtained with other sampling Iron-scintillator calorimeters with conventional geometries.

5.4.3 e/π response, longitudinal sampling corrections and linearity

The e/π response of a sampling calorimeter with an Iron/scintillator ratio less than 20 is expected [7] to be > 1 for the conventional orientation of tiles with respect to incident hadrons. The e/π response of the prototype under study has been calculated by dividing the mean electron response, obtained in section 5.3, by the peak values of the hadron energy spectra. The resulting e/π ratios as a function of energy are given in Figure 16 for electrons and pions incident at 20^0. The ratios are in the range of 1.2 to 1.1, a relatively small deviation from the ideal "compensation", which helps in qualitatively understanding the lack of high-energy tails in the hadron energy spectra which was pointed out above.

It is well known that $e/\pi \neq 1$ causes deviations from linearity in the hadronic response *vs.* energy, besides broadening the energy resolution. Experience from previous longitudinally segmented calorimeters [8] [9] suggested to try longitudinal sampling corrections in order to improve both aspects of the performance of the prototype calorimeter. The strategy in choosing a correction algorithm has been to compensate for $e/\pi > 1$ by adjusting downwards the response of readout cells with large signals, due to electromagnetic energy clusters, by means of a minimal set of energy-independent parameters. This strategy is physically well motivated [8] and can therefore be expected to yield the minimal number of parameters. For the same reason this method can also be expected to improve the linearity of the calorimeter response.

The following form was found to effectively correct for electromagnetic shower fluctuations, with negligible dependence on incident particle energy:

$$Q_{ij}^{corr} = Q_{ij}(1 - \frac{P_j}{Q_j}.Q_{ij})$$

where Q_{ij} is the (charge) signal in each readout cell, with index i for the tranverse segmentation (i =1 to 15, including all 3 modules) and index j for the

longitudinal segmentation (j =1 to 4), and Q_j is the sum of the signals in the 15 cells comprizing a longitudinal segment. The denominator Q_j effectively makes the correction dependent on the fraction of the signal in one cell relative to the deposit in the entire longitudinal segment. The parameters P_j are in principle four; however it was found that $P_2 = P_3$ within errors, and that setting $P_4 = 0$ made no difference to the resolution (apparently because of the effect of longitudinal leakage at the higher energies); therefore the correction to the cell energies were calculated with only two parameters, which were empirically determined for the 10^0 and 20^0 data. The parameters P_1, P_2 are in the range 0.2 to 0.3 at both incidence angles.

The overall corrected pion signal $Q^{corr} = \Sigma Q_{ij}^{corr}$ was found to be remarkably linear *vs.* beam energy, but with negative intercept at $E_{beam} = 0$. Therefore the final corrected energy is obtained (at the price of a third parameter) as

$$Q^{corr} = q + \Sigma Q_{ij}^{corr}$$

The value of q giving the best proportionality to beam energy is 10 pC, or about 1.7 GeV.

In summary, the pion response of the calorimeter has been corrected using only three energy-independent parameters, which are weakly dependent on the hadron incidence angle. The σ/E resolutions *vs.* $1/\sqrt{E}$ for the raw and the corrected spectra are given in Figure 17 for the 10^0 and 20^0 data; the numerical values are in Table 1.

In the energy dependence of the resolutions the statistical term (dominated by sampling fluctuations) is unaffected by the longitudinal weighting procedure, but the constant term is reduced to about 1.3%; this confirms that the method effectively corrects the fluctuations of the fraction of electromagnetic energy in the hadronic shower [7].

Finally, the linearity of the raw and uncorrected pion signals are compared in Figure 18. Raw and corrected charge/E_{beam} ratios are normalized to the value at 20 GeV. The ratios formed with the raw data show an approximately logarithmic rise with energy, in accord with previous parametrizations of the electromagnetic energy fraction. After correction, the ratios show an *r.m.s.* deviation from linearity 0.6% at 10^0 and 1.2% at 20^0.

6 Conclusions and Future Prospects

The first prototype of a sampling calorimeter with a longitudinal tile configuration has been built and tested with muon, electron and pion beams.

Prototype construction and beam tests were performed over a period of 6 months; the construction of three test modules proceeded smoothly and confirmed that the mechanical and optical concepts will allow economical construction of a large detector for LHC physics.

Fits to raw spectra				
E_π *(GeV)*	10°		20°	
	$<Q>$ *(pC)*	σ *(pC)*	$<Q>$ *(pC)*	σ *(pC)*
20	109.2 ± 0.3	14.89 ± 0.27	112.5 ± 0.3	14.31 ± 0.27
40	229.1 ± 0.4	22.58 ± 0.39	231.3 ± 0.4	22.00 ± 0.41
80	469.5 ± 0.7	37.09 ± 0.64	468.3 ± 0.7	35.24 ± 0.62
150	903.3 ± 1.1	58.30 ± 1.04	905.7 ± 1.1	54.41 ± 1.00
200	1211 ± 1.4	72.53 ± 1.30	1213 ± 1.3	67.42 ± 1.18
300	1836 ± 2.0	95.73 ± 1.84	1844 ± 1.9	89.95 ± 1.69
Fits to corrected spectra				
E_π *(GeV)*	10°		20°	
	$<Q>$ *(pC)*	σ *(pC)*	$<Q>$ *(pC)*	σ *(pC)*
20	103.3 ± 0.3	12.54 ± 0.25	109.9 ± 0.3	12.28 ± 0.24
40	204.3 ± 0.4	18.05 ± 0.33	214.2 ± 0.4	18.09 ± 0.36
80	406.5 ± 0.6	27.87 ± 0.58	424.2 ± 0.6	28.17 ± 0.54
150	767.3 ± 0.8	40.14 ± 0.74	808.4 ± 0.8	40.87 ± 0.79
200	1024 ± 1.0	49.56 ± 0.91	1080 ± 1.0	46.12 ± 1.00
300	1542 ± 1.3	62.84 ± 1.23	1631 ± 1.4	64.29 ± 1.29

Table 1: Peak and σ values from fits to raw and corrected pion energy spectra

The calibration tools implemented show that such a calorimeter can be precisely and reliably intercalibrated.

The results from the test beam show that the hadron energy resolutions are competitive with those obtained with conventional sampling Iron calorimeters, even when the calorimeter is exposed to hadrons without an upstream EM compartment.

The resolutions obtained in such a standalone mode can be further improved with a simple longitudinal sampling correction procedure, which has the important additional benefit of yielding a very good linearity versus incident hadron energy.

Extensive studies [10] conducted within the collaboration have shown that

this calorimeter can tolerate a radiation exposure equivalent to at least 10 years of operation at the LHC design luminosity with negligible radiation damage.

Based on these results the ATLAS collaboration [11] has chosen to build a hadron calorimeter according to this design in the pseudorapidity region $-1.6 \leq \eta \leq 1.6$. The calorimeter being designed for ATLAS will have about 10000 readout channels and will weigh approximately 2500 tons.

Further R&D, data analysis and engineering studies are in progress, to improve some performance aspects, optimize the design of the ATLAS calorimeter, and identify the most economical construction options.

The specifically instrumental developments include the following subprojects:

1. Studies and optimization of the scintillator optical characteristics: some dependence of the signal on the impact point of the particle along the $r \times \phi$ coordinate has been observed and is under further study. The observed behavior appears to depend on light attenuation in the scintillator and on the detailed shape of the scintillating tile.

2. Fiber response to ionizing particles: such a response has been observed, and can be minimized by suitable additions to the fiber materials.

3. Photoelectron yield: the measured yield is not an important contributor to the hadron resolution, however a larger yield would provide a better safety margin. A commercial multi-clad fiber has already been shown in beam tests to provide an improvement factor of 1.6 in photoelectrons/GeV.

4. Choice of the readout PMT: a commercial photomultiplier of optimal dimensions and reduced sensitivity to magnetic fields has been found.

In the near future, the prototype calorimeter will be augmented to 5 modules and placed in a test beam downstream of a prototype of the ATLAS Barrel liquid Argon EM calorimeter. This will be the first test of the ATLAS hybrid hadron calorimeter.

Acknowledgements

The construction of the calorimeter prototype within a very short time was only possible with the substantial contribution of the collaborating Institutes' technical staff. We deeply thank them for their support; we are particularly grateful to L. Bonnefoy, J.M. Chapuis, C. Fayard, S. Mayade, L. Rose-Dulcina, E. Sahuc, R. Saigne, G. Sannier, G. Savinel and A. Siegrist.

We are indebted to V. Barnes from the University of Notre Dame who lent us the ^{137}Cs source with its mechanical drive and associated electronics, which made it possible to develop the source calibration method in time for the test beam runs.

Financial support is acknowledged from the funding agencies of the collaborating Institutes.

References

[1] O. Gildemeister, F. Nessi-Tedaldi, M. Nessi, " An economic concept for a barrel hadron calorimeter with iron scintillator sampling and WLS-Fiber readout ", Proceedings of the Second International Conference on Calorimetry in High Energy Physics, Capri, 1991, page 189.

[2] D. Acosta *et al.*, Nucl. Instr. and Meth. **A308** (1991) 481.

[3] B. Aubert *et al.*, Nucl. Instr. and Meth. **A321** (1992) 467.

[4] M. Bosman *et al.*, (RD34 Collaboration), " Developments for a scintillator tile sampling hadron calorimeter with longitudinal tile configuration ", CERN/DRDC/93-3 (1993).

[5] E. Moyal, Phil. Magazine **46** (1955) 263.

[6] J. Badier *et al.*, Nucl. Instr. and Meth. **A337** (1994) 314, and 326.

[7] R. Wigmans, Nucl. Instr. and Meth. **A259** (1987) 389.

[8] H. Abramowicz *et al.*, Nucl.Instr. and Meth. **180** (1981) 429.

[9] M De Vincenzi *et al.*, Nucl. Instr. and Meth. **A243** (1986) 348.

[10] A. Amorim *et al.*, " Study of the effect of radiation on the TILECAL Barrel hadron calorimeter to be used in ATLAS", Proceedings of the Fourth International Conference on Calorimetry in High Energy Physics, Elba, 1993 and ATLAS Internal Note TILECAL-NO-002.

[11] The ATLAS Collaboration, Progress Report on ATLAS Milestones, CERN/LHCC/93–51, Oct. 1993.

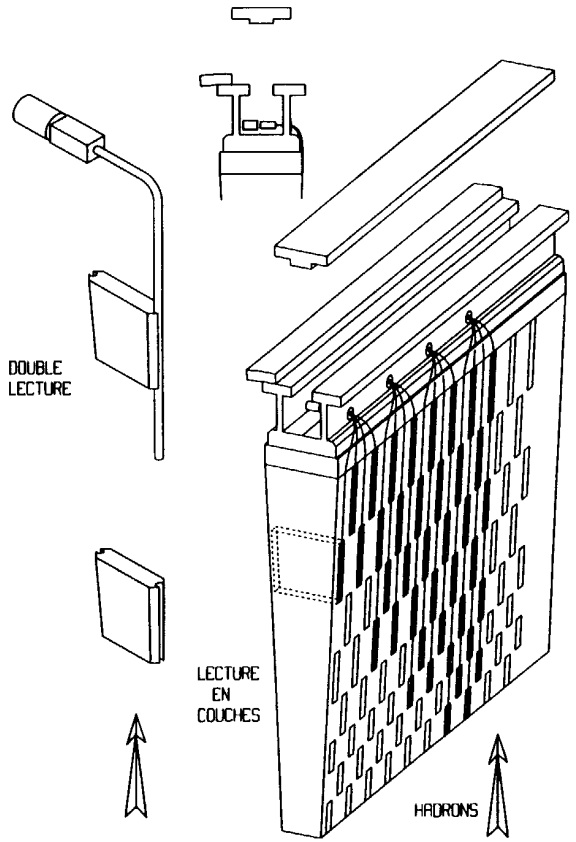

Figure 1: Principle of the proposed hadron calorimeter.

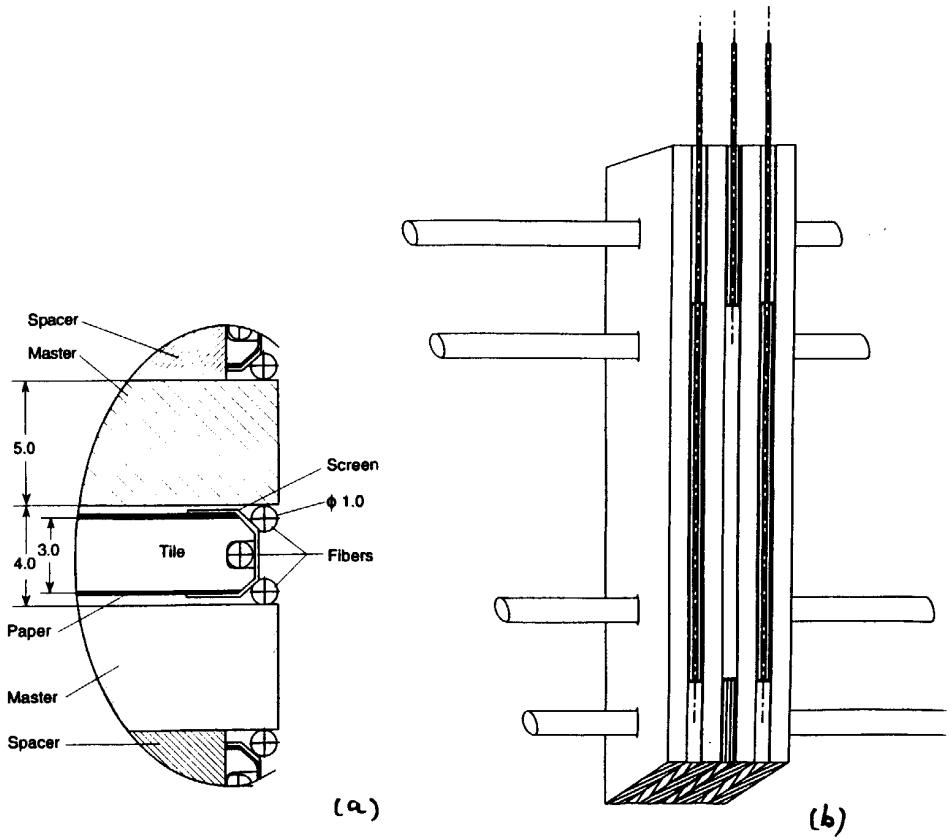

Figure 2: (a): detail of the coupling between scintillator and WLS-fiber; (b): view of the calorimeter layers, including master and spacer plates, scintillator, fibers and rods.

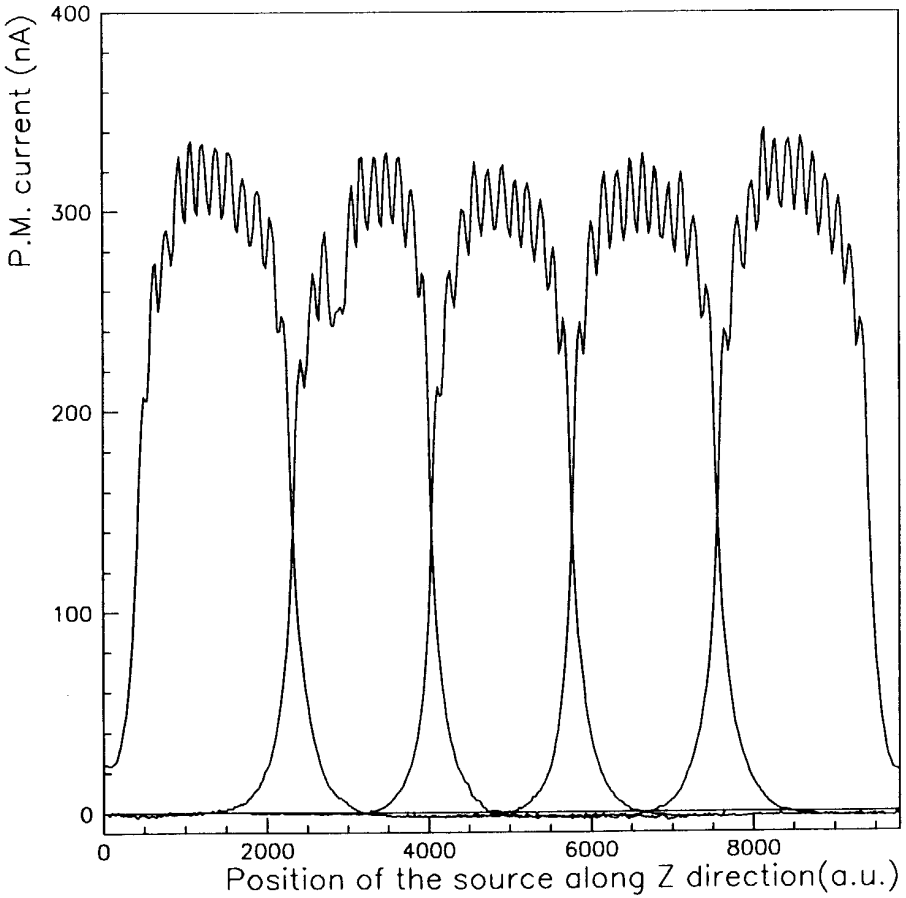

Figure 3: Current measured in the PMTs as a function of the position of the source along the rod (z axis).

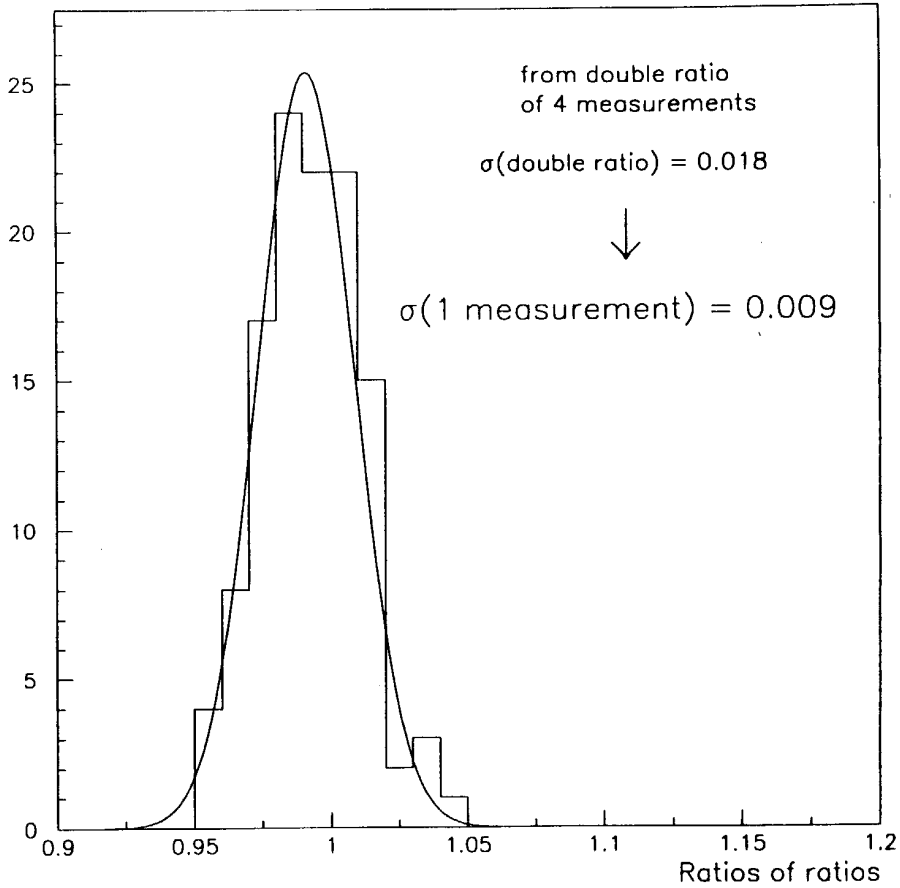

Figure 4: Reproducibility of the source calibration inferred from double ratios of measurements.

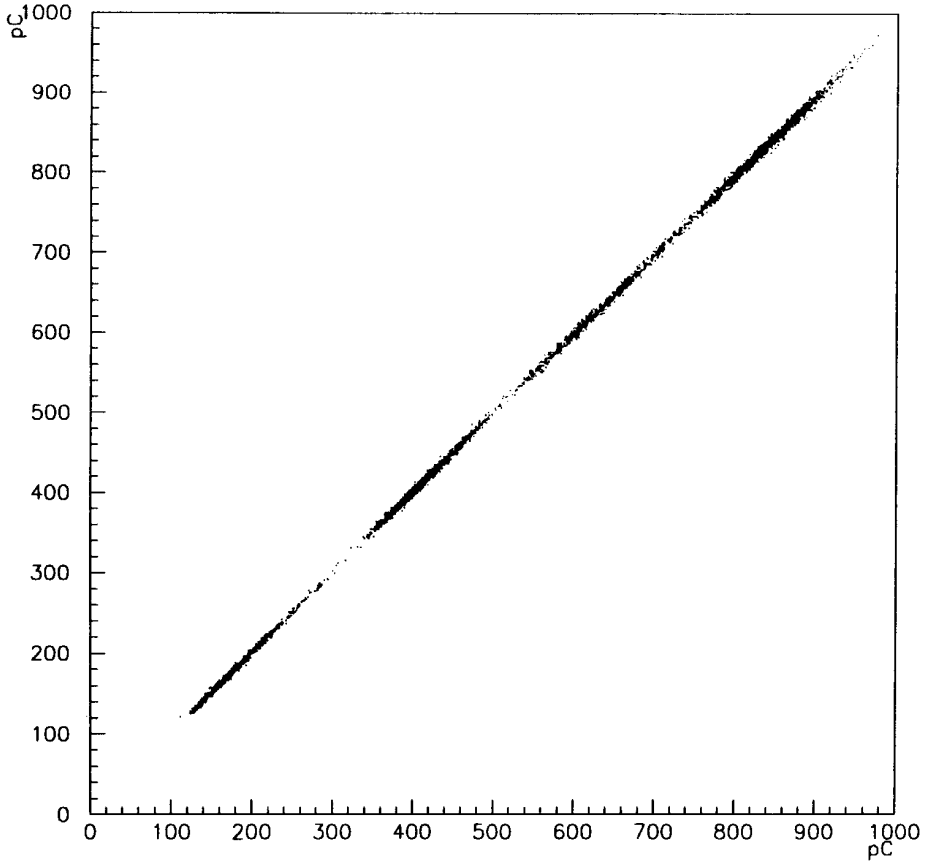

Figure 5: Laser intensity monitoring: correlation of the charges measured by the two monitoring diodes.

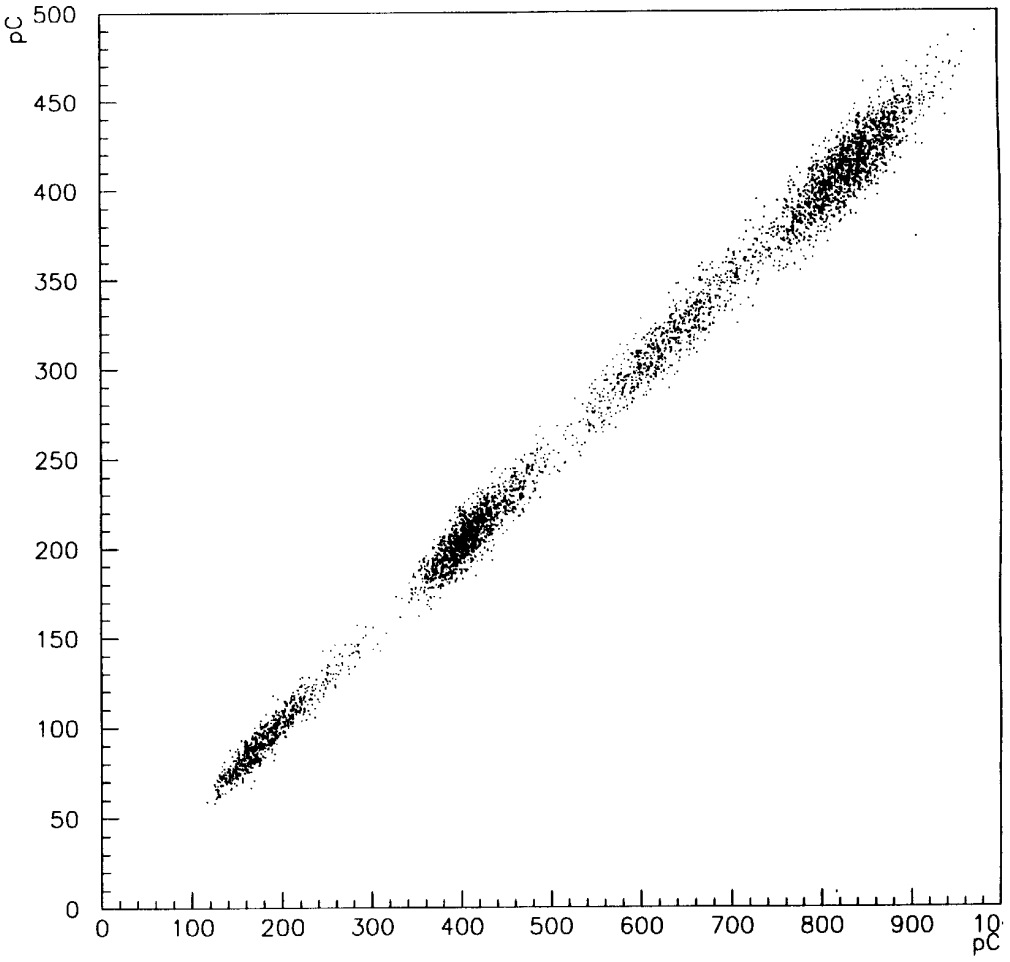

Figure 6: Laser monitoring of the PMT response: PMT charge signal *vs.* mean of diode monitor signal.

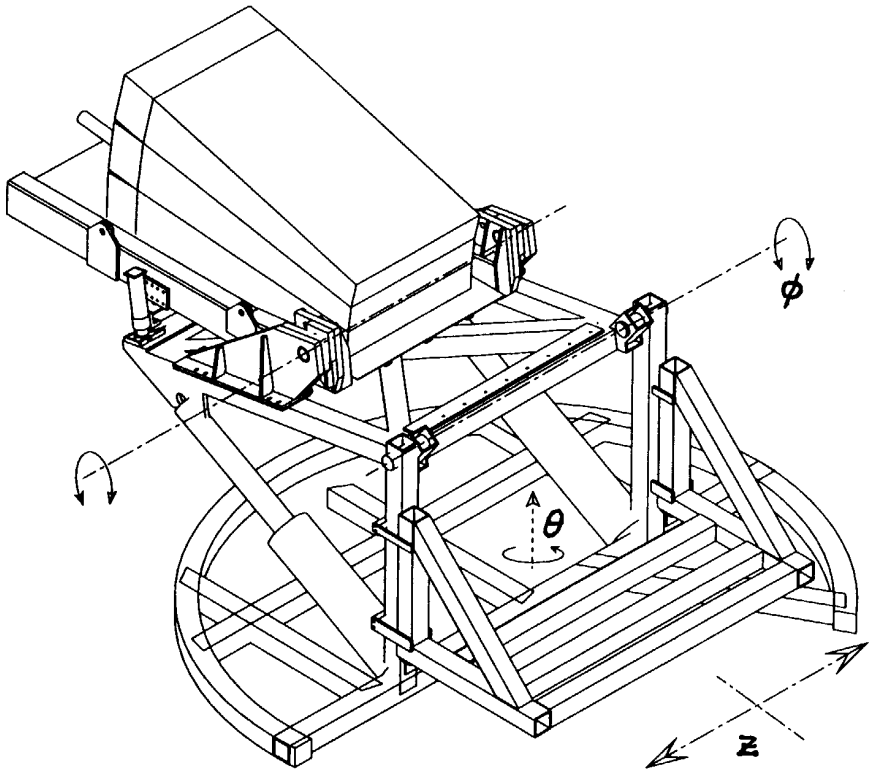

Figure 7: View of the scanning table, with three prototype modules. The three movements (z, θ, ϕ) are shown.

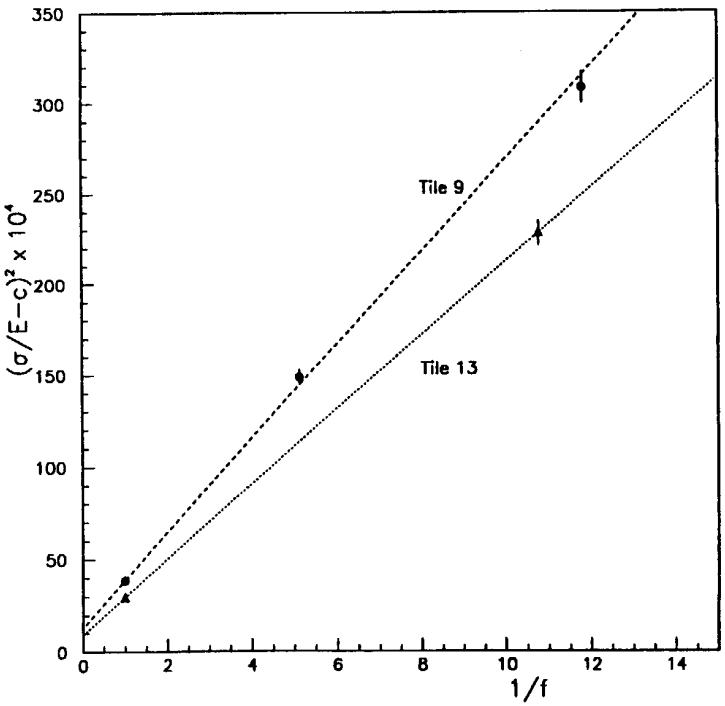

Figure 8: Tile calorimeter light yield: measurements for two tiles and several filter attenuation factors f.

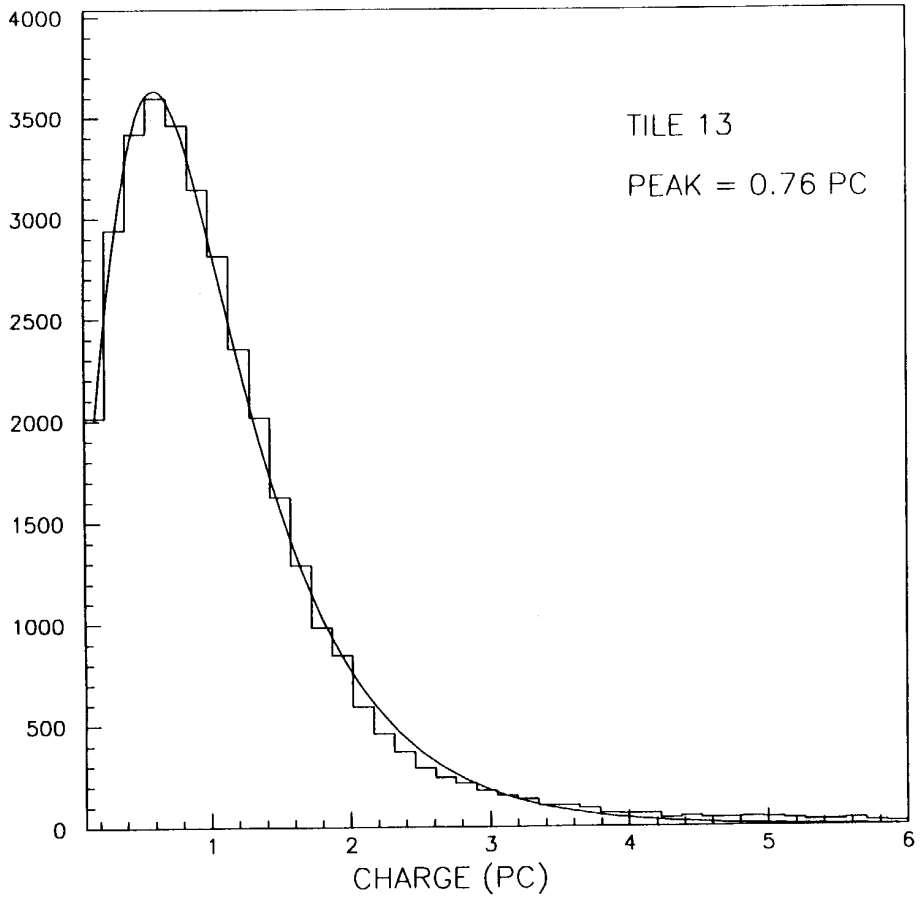

Figure 9: Individual cell signal distribution for 225 GeV muons traversing the calorimeter at an incidence angle $\theta = 90^0$.

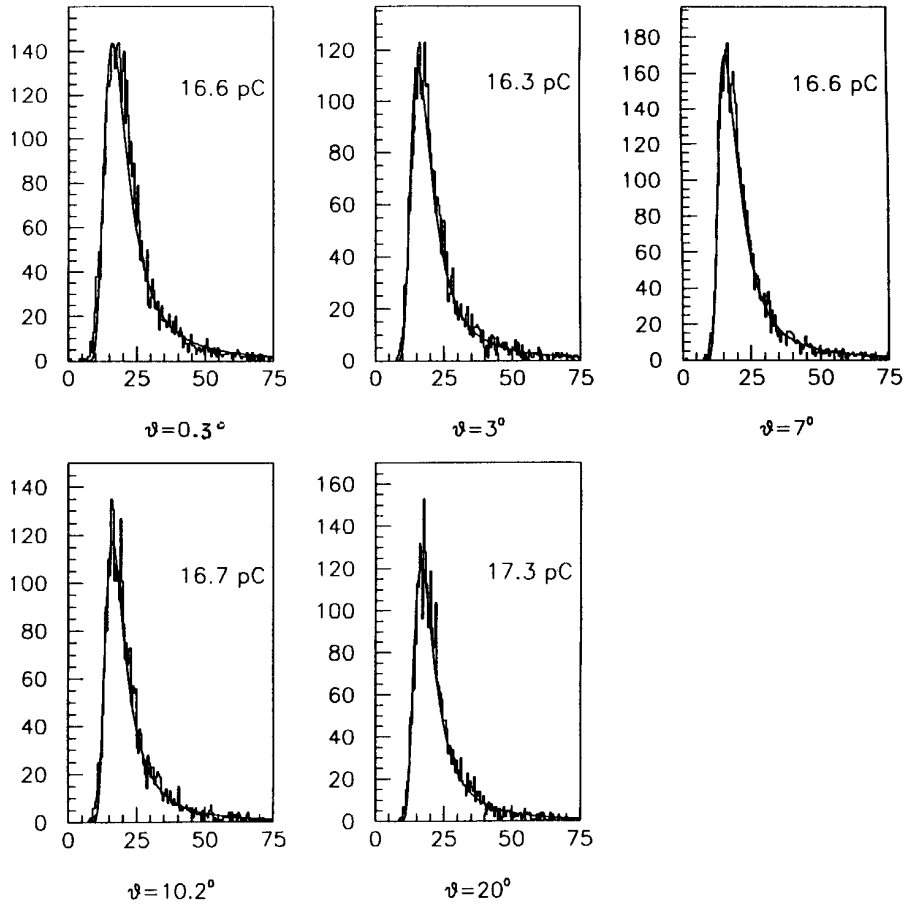

Figure 10: Signal distributions for 225 GeV muons at incidence angles of 0.3^0 to 20^0; the signal in the entire calorimeter (4 longitudinal segments) is shown.

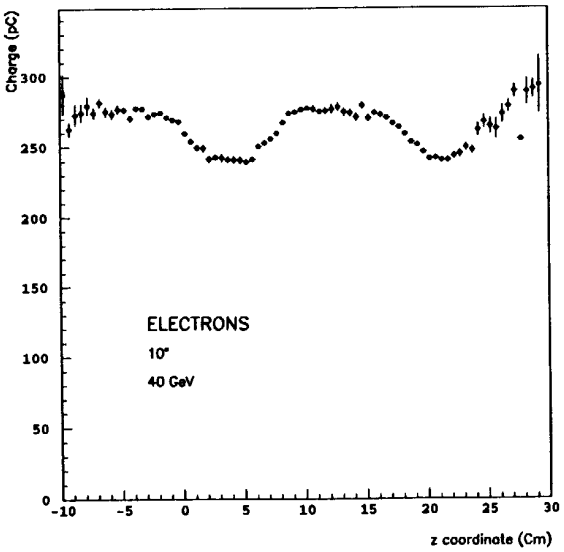

Figure 11: Response to 40 GeV electrons at 10^0. The mean signal in 1 mm bins (z coordinate) is shown over several periods of 18 mm.

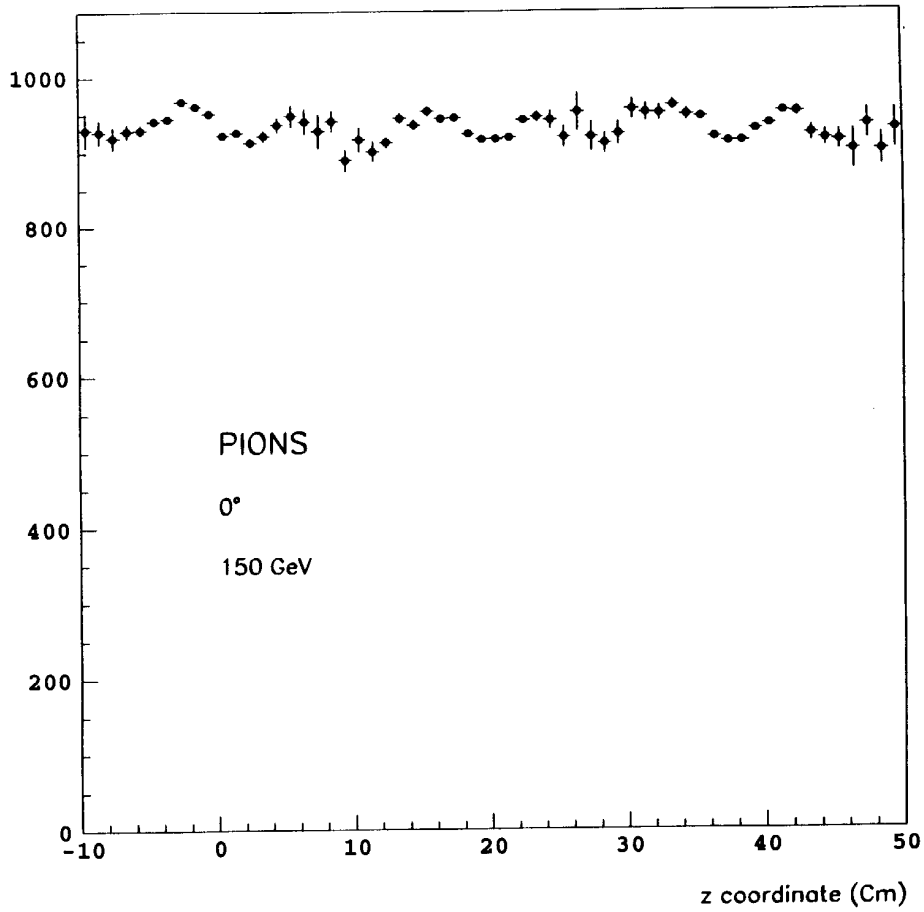

Figure 12: Response to 150 GeV pions at 0^0. The mean signal in 1 mm bins (z coordinate) is shown over several periods of 18 mm.

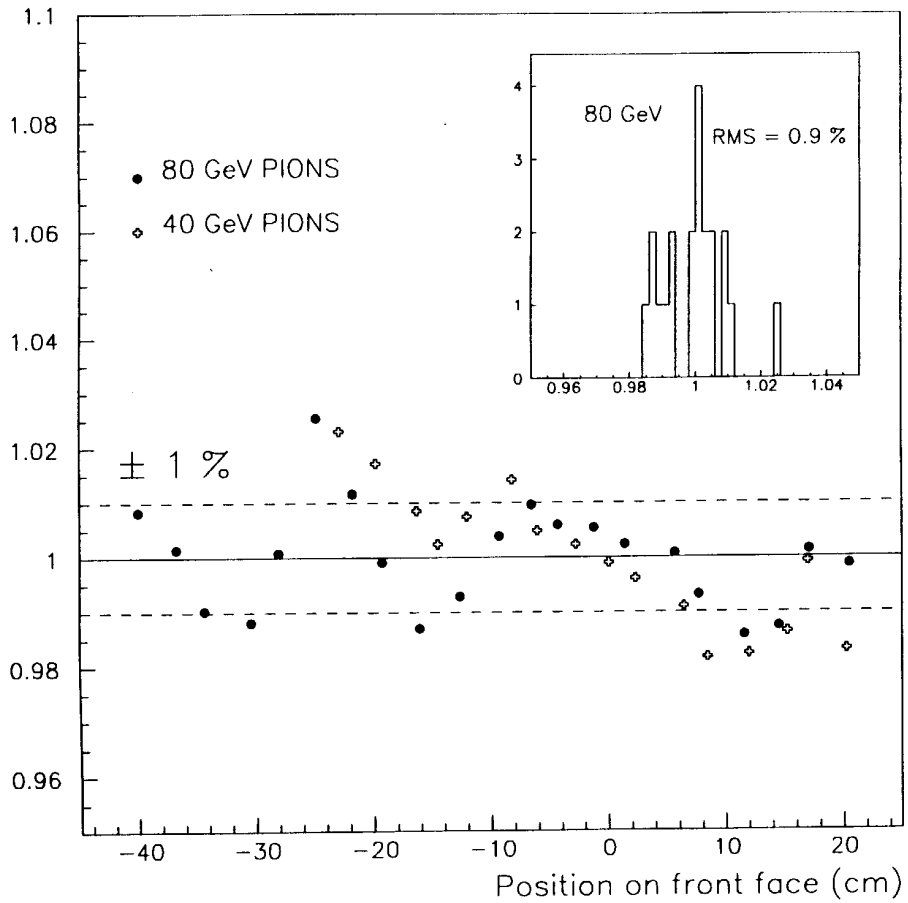

Figure 13: Uniformity scan with 40 and 80 GeV pions at 10^0. The insert shows the distribution of the signal (peak) for the 21 points at 80 GeV.

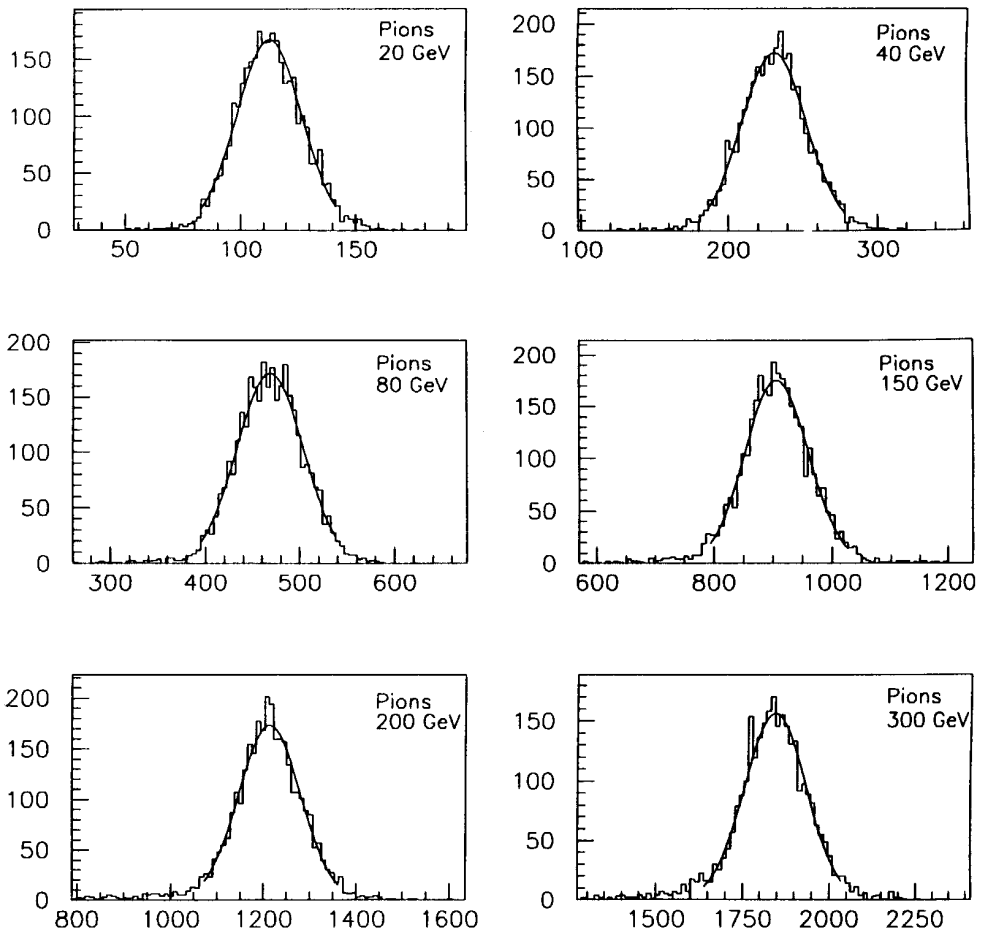

Figure 14: Raw pion energy spectra at 20^0. The gaussian fits are over $\pm 2\sigma$; the results of the fits are given in Table 1.

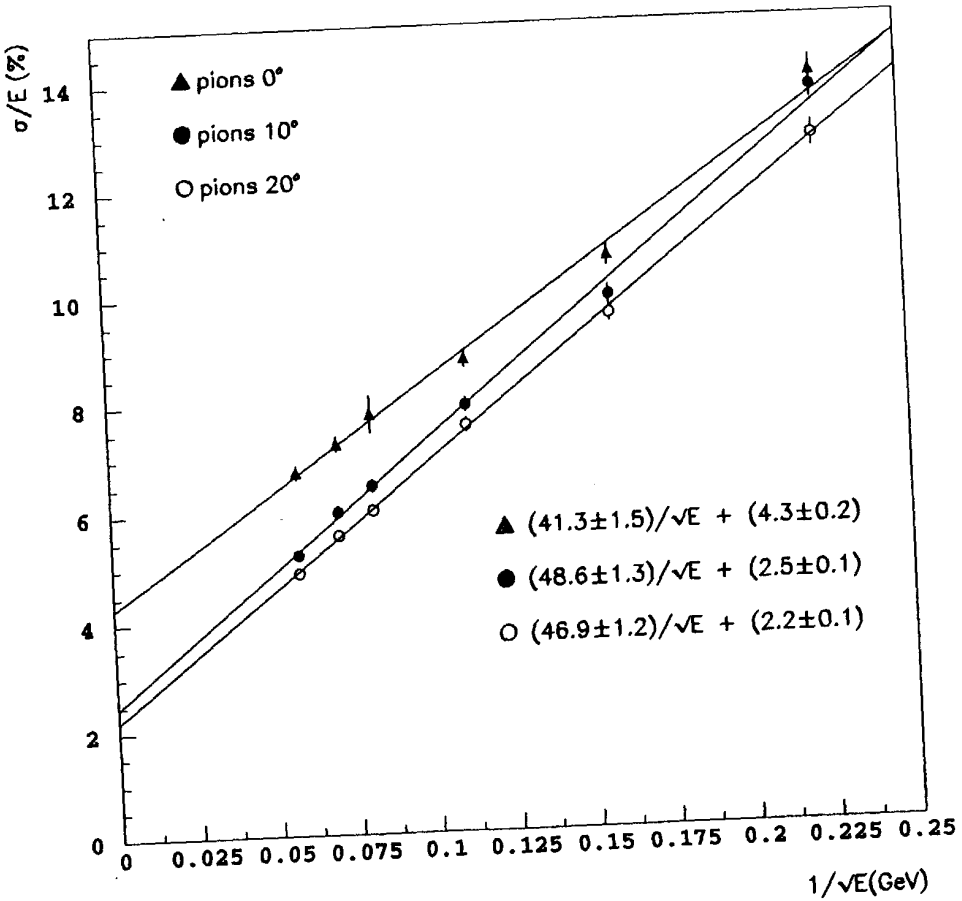

Figure 15: Energy resolutions σ /E *vs.* $1/\sqrt{E}$ for pions at 0^0, 10^0 and 20^0.

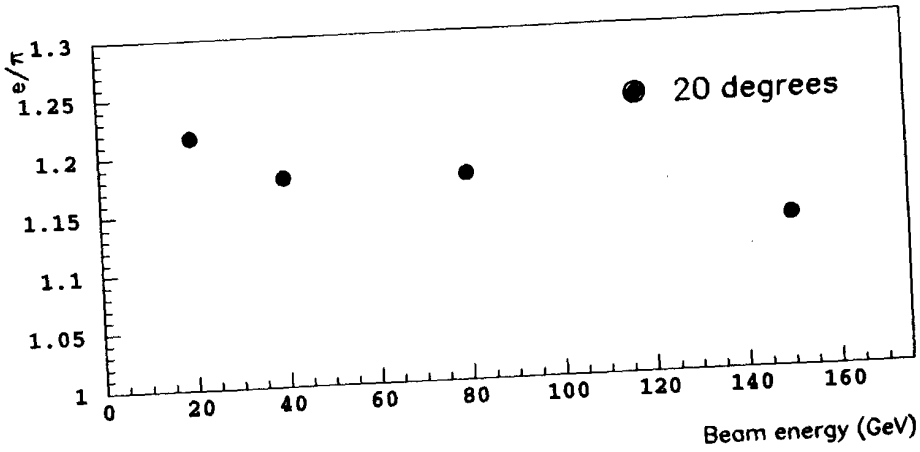

Figure 16: e/π ratio at 20^0 for 20 $GeV \leq E \leq 150GeV$.

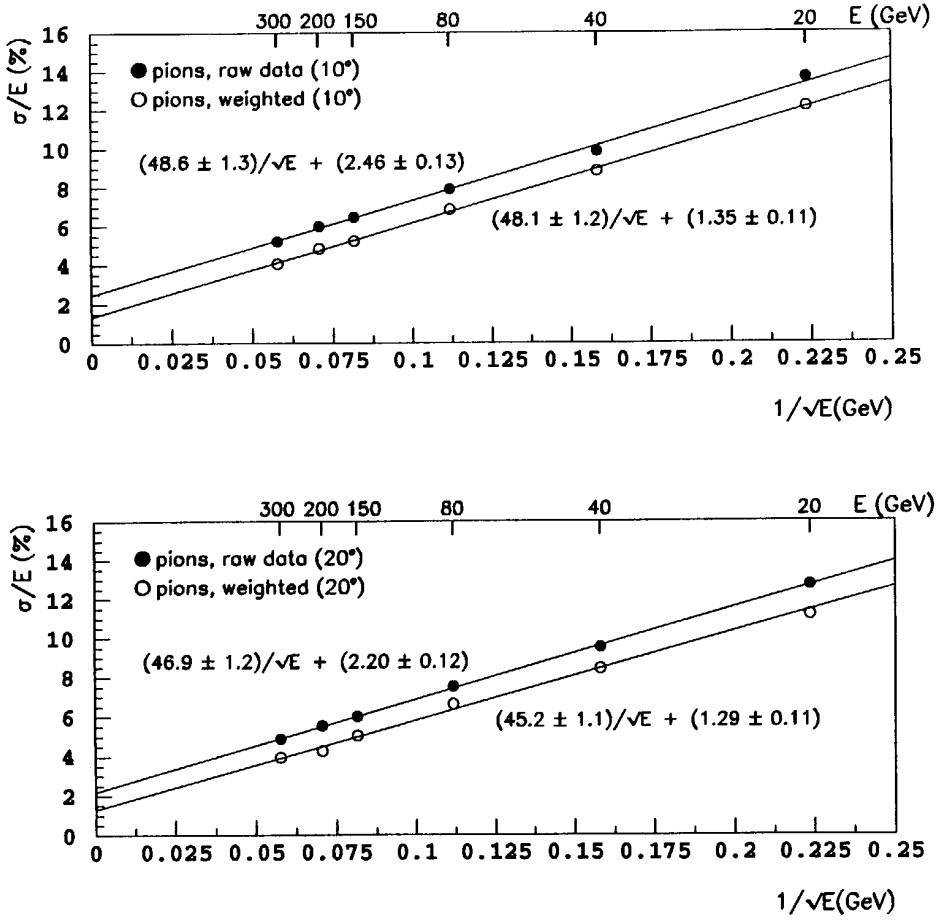

Figure 17: Pion energy resolutions, for raw and corrected energy spectra, *vs.* $1/\sqrt{E}$. Separate plots for 10^0 and 20^0 data.

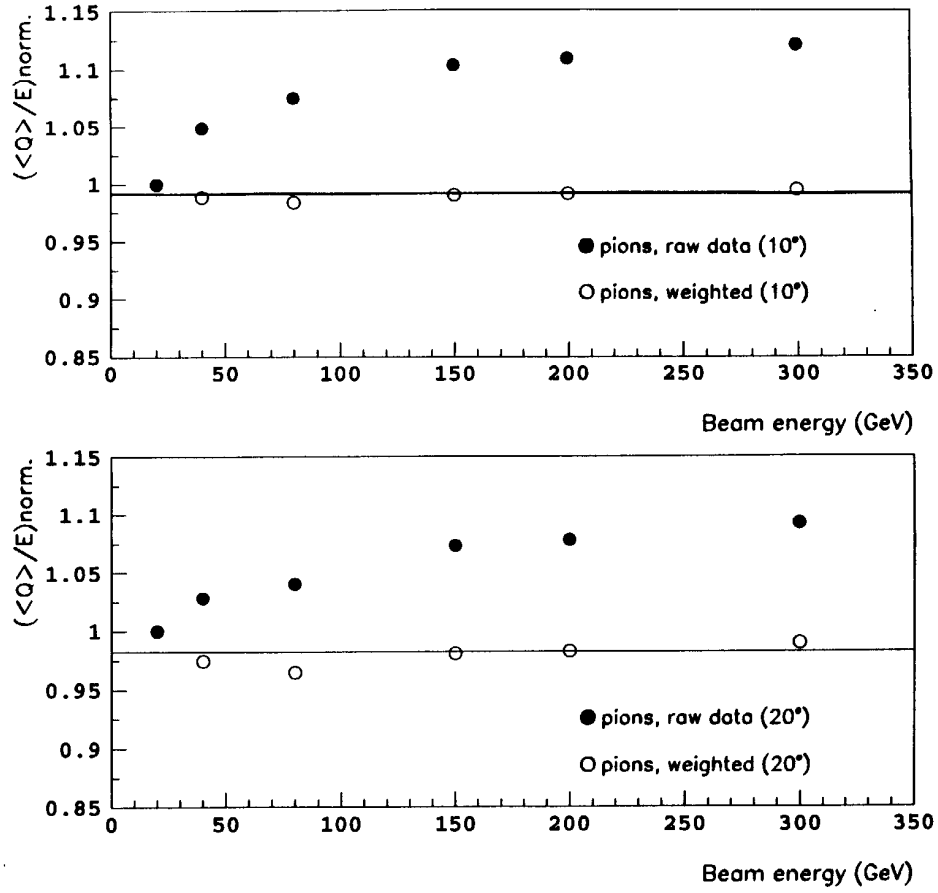

Figure 18: Response to pions (ratio of peak charge from gaussian fits to beam energy, normalized to values at 20 GeV) from raw and corrected energy spectra. Separate plots for 10^0 and 20^0 data.

7 Appendix :

ATLAS Internal Note
TILECAL-NO-002
13 December 1993

Study of the effect of the radiation on the TILECAL Barrel hadron calorimeter to be used in ATLAS

(Presented by Ana Henriques-In the framework of the RD34 collaboration)

A. Amorim[1,2], M. David[1,2], A. Gomes[1,2], A.Henriques[3], A. Maio[1,2]

1- LIP/Lisbon ; 2- University of Lisbon ; 3- CERN

Abstract

The effects of radiation damage induced by neutrons and charged particles on the performance of a TILECAL Barrel hadron calorimeter are studied. For an integrated luminosity of $10^6 pb^{-1}$ (10 years running at a peak luminosity of $1.6x10^{34}cm^{-2}s^{-1}$) the degradation on the jet energy resolution and the total light reduction are marginal, even when the 4 longitudinal sectors of the calorimeter are not periodically recalibrated. The largest effect is observed in the light reduction on the first tile, starting at 1.95λ, and it is is 6.2% at $\eta = 1.5$ and 4.8% at $\eta = 0$. In the most exposed Barrel region ($\eta = 1.5$) the increase on the jet energy resolution of 300 GeV incident jets is 0.24% without longitudinal calibration and 0.16% when the calibration is applied. The total signal is reduced by 1.51% without calibration and 0.14% after calibration.

1. Dose Levels Expected in the Barrel Hadron Calorimeter in ATLAS.

The expected annual peak dose in the ATLAS barrel hadron calorimeter coming from charged particles and neutron fluxes (E_n > 100 keV) is 36 Gy/y[1,2,3], considering a 5 cm polyethylene moderator in front of the LAr/Pb e.m. calorimeter and followed by a iron/plastic scintillator hadron calorimeter.

This dose has been obtained from a more general ATLAS setup: a mean medium in the calorimeters (LAr/Pb in the e.m. calorimeter and LAr/Iron in the had. calorimeter)[2,3]. In the case of a iron/plastic scintillator calorimeter with a ratio of 4.5 to 1 (TILECAL), the dose induced by neutrons and charged particles in the plastic scintillator is higher and has been corrected for.

1.1- Corrections applied to the doses induced by neutrons

Neutrons produced in the hadronic shower will have a large $\sigma_{elast.}$ to elastically scatter off the protons in the plastic scintillator of the TILECAL calorimeter. The neutron capture in Hydrogen is negligible with respect to the elastic scattering in the full energy range[5].

A relation between an integrated neutron fluence F_n (n/cm^2) and the induced dose deposited in the plastic (Gy) considering only elastic processes (σ_{elast} in cm^2) is given by [6]:

$$(Dose)_n = F_n \frac{N_0\, \sigma_{elast}}{A} \frac{<E>}{2} \qquad (1)$$

where $N_0 = 5.2x10^{25}$ protons.kg^{-1}, A = 1 and <E>/2 is the mean energy (in J) of the proton recoil after elastic scattering. In the case of a mean medium of Fe/LAr (A>> 1) there is a negligible neutron contribution to the total dose.

The contribution of neutrons to the doses deposited in the plastic scintillator will be calculated directly from the neutron fluxes expected in the barrel hadron calorimeter . Only the fast (E_n > 100 keV) fluxes with a 5 cm polyethylene moderator in front of the LAr e.m. calorimeters, e.g. $1.0x10^{12}$ n/cm^2 were considered. This value is reduced 14% when the LAr is

replaced by plastic in the hadron calorimeter[3]. For one year running (10^5 pb^{-1}), the expected fast neutron peak flux in the plastic scintillator ((1-0.14)x10^{12} n/cm^2) corresponds to a peak dose $(Dose)_n$ = 9.6 Gy/y if we consider <E> = 300 - 400 keV, the energy at which the neutron flux is maximal[4] (see more details in ref. 1). For smaller neutron energies the corresponding dose will be much smaller (see table 1). The contribution of the neutrons with $E_n \leq 100$ keV to the dose is then negligible with respect to the fast neutrons.

Table 1- Values of $\sigma_{elast.}$.<E> for several neutron energies.

E_n (MeV)	$\sigma_{elast.}$ x <E> (b.MeV)	Contribution to the dose normalized to 1 MeV
1	4	1
0.3-0.4 (max. flux)	2.8-2.4	0.7-0.6
0.01	0.19	4.8x10^{-2}

1.2. Corrections applied to the doses induced by charged particles and π^0's.

In TILECAL, the dose deposited in the plastic by $\pi^{\pm}$'s is higher than the values given for a mean medium of Fe/LAr by a factor roughly proportional to $[(dE/dx_{scint})/(dE/dx_{<Fe/LAr>})]$ = $[(dE/dx_{scint})/(dE/dx_{Fe})]$ = 1.3. We keep the total amount of the doses given for a mean medium (10 Gy/y and 20 Gy/y for η = 0 and η = 1.5 respectively) assuming that they are only coming from charged particles. The peak doses in the active medium of the TILECAL calorimeter induced by charged particles are then 13 Gy/y and 26 Gy/y for η = 0 and η = 1.5 respectively.

1.3. Final Doses after 10 years working at a peak luminosity of 1.6x10^{34}cm^{-2}s^{-1}(10^6pb^{-1})

For an integrated luminosity of 10^6pb^{-1} the expected peak doses (n + π's) deposited in the plastic scintillator of the TILECAL calorimeter are given on table 2 for η = 0 and η= 1.5 with rather conservative assumptions. The variation of the doses with the hadronic calorimeter depth are shown on fig. 1.

Table 2- Peak doses (Gy) expected in the plastic scintillator of the barrel had. calorimeter from charged particles and neutrons after an integrated luminosity of 10^6pb^{-1} for η = 0 and η= 1.5.

η	Dose Charg. particles (Gy)	Dose neutrons (Gy)	Total Dose (Gy)
0	130	96	226
1.5	260	96	356

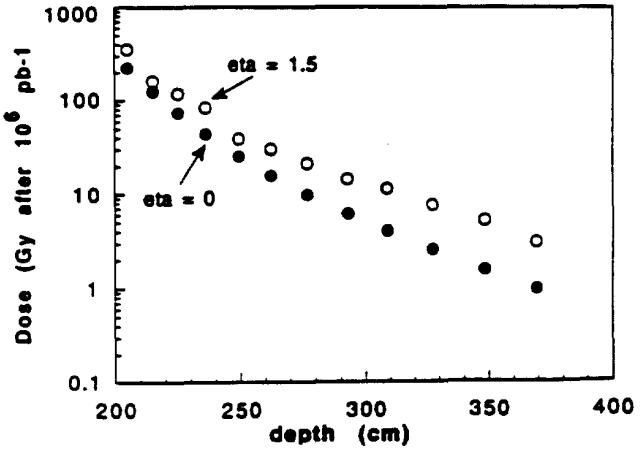

Fig. 1- Total doses (n+π's) in Gy expected in the TILECAL after 10^6pb^{-1} for η= 0 and η = 1.5, as a function of the hadron calorimeter radial depth (see more details in ref. 1).

2. Radiation Hardness of a Tile/WLS fibre calorimeter considering the SDC and TILECAL configurations.

Due to the absence of complete experimental results concerning irradiation in the exact TILECAL configuration, the SDC experimental radiation damage results were used to evaluate the light reduction as a function of the dose, since this is the closest configuration to the TILECAL calorimeter. In fig. 2 is shown the light ratio (before/after irradiation) as a function of the dose in Mrad (1 Gy = 100 rad) at the maximum of the shower induced by 2.5 GeV electrons in a SDC module[7]. The data from 3 different modules fit well with a 2 exponential curve:

$$I/I_0 = 0.824\ e^{-D/\gamma 1} + 0.157\ e^{-D/\gamma 2} \quad \text{with } \gamma_1 = 43000\,\text{Gy}\ ;\ \gamma_2 = 1350\,\text{Gy} \qquad (2)$$

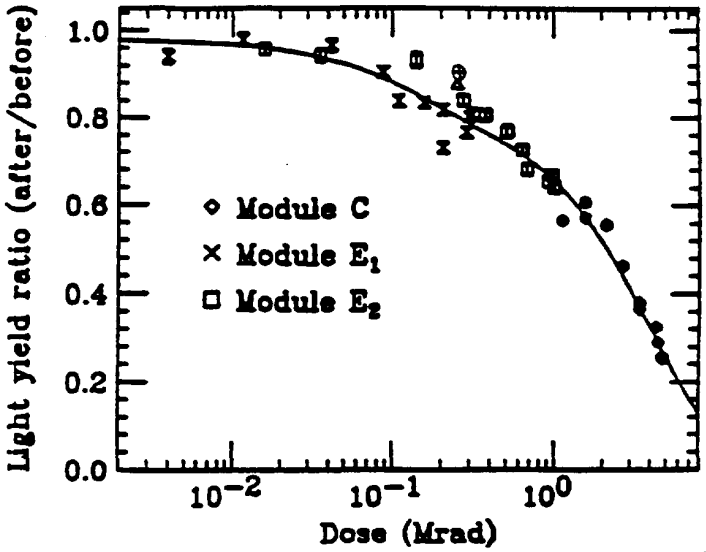

Fig. 2 Light yield ratio after irradiation at shower maximum for SCSN81(tiles)/Y7(WLS fibres) modules as a function of the dose at the shower maximum[7]. The ♦, x and ◻ points correspond to 3 different modules.

Preliminary results obtained by irradiating in a γ-^{60}Co source several tile/WLS fibre assemblies* in the exact TILECAL configuration[2] show very encouraging results, which we describe next: PSM-115 tiles of 200x100x3 mm^3 and 350x100x3 mm^3 have been irradiated to a dose of 2.75 kGy with a maximum dose non uniformity of 10%. The fibres (1.5 m long) were irradiated with a constant dose of 2.2 kGy in the last 1 meter[9]. The first 0.5 m length received a nigligible dose**. This is a pessimistic situation since we expect a logarithmic decrease of the dose as a function of the fibre depth (fig. 1). The dose rate was 16 Gy/hour.

The light output of each tile/fibre assembly was measured with a ^{90}Sr source before and after irradiation, doing a scan with the source in the middle of the tile along the longest dimension. Two fibres of the same quality placed in the grooves made in the two far oposite extremities of the tile[2] are used in the measurements. The light output of 2 tile/fibre assembly types (PSM-115/BCF91A and PSM-115/Y11(200ppm)M) is shown in fig. 3a and 3b respectively.

**Tile type: PSM-115 (granulated polysterene base doped with 1.5% PTP and 0.03% POPOP). They are processed by injection molding technology in Protvino laboratory.*
Fibres types: BCF91A from Bicron and Y7(150ppm), Y7(150ppm)N (new cladding), Y11(200ppm), Y11(200ppm)M (double cladding), Y11(100ppm)M (double cladding) from Kuraray.

*** Considering the origine the end of the fibre that will be read out by the PMT.*

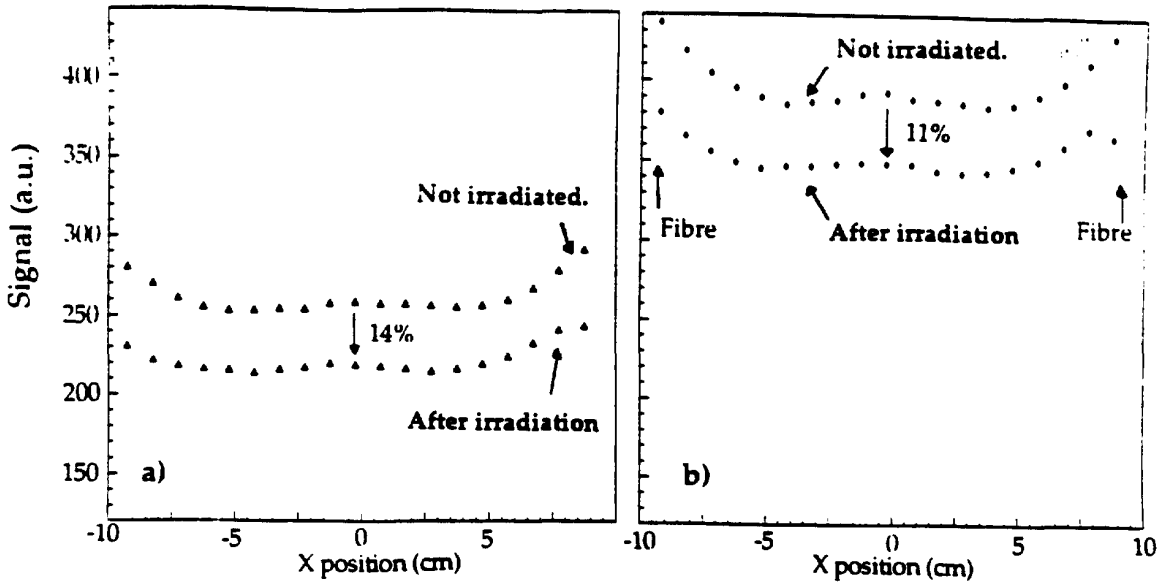

Fig. 3- Light output as a function of the x position for 2 tile/fibre assembly types a) PSM-115/BCF91A and b)PSM-115/Y11(200ppm)M), before and after irradiation in a ^{60}Co source at a dose of 2.75 kGy.

We observe that before irradiation the light output using the Y11(200ppm)M fibre pair is higher by about a factor of 1.5 with respect to the BCF91A fibre pair. This is mainly because the Y11(200ppm)M fibre has a double cladding (index of refraction n_{core} = 1.59, $n_{clad\ 1}$ = 1.49, $n_{clad\ 2}$ = 1.42) which improves the light reflection in the core-cladding surface and increases the numerical aperture[10]. The light reduction after irradiation is about the same in both cases within the experimental errors. When the BCF91A fibres are used we observe a light reduction after irradiation of 14%, and 11% for the Y11(200ppm)M fibres.

The Δ and ⊕ points in fig. 2 for a dose of 2.75 kGy (0.275 Mrad~100 years working at LHC) correspond to the two TILECAL tile/fibre configuration assemblies (fig. 3), showing good agreement with the SDC results. The light reduction in the fibres is the major contribution to the global light reduction of the tile/fibre assemblies due to the non realistic fibre dose profile applied, mentioned before. This was confirmed redoing the scan of fig. 3a using the same tile but non irradiated BCF91A fibres. In this case a light reduction of 3.5% is observed.

The light attenuation curve of each individual fibre was also measured before and after irradiation. The light output ratio of each individual fibre type measured at a distance of 130 cm from the PMT over the signal measured at a distance of 40 cm from the PMT is shown in table 3 after normalizing to the respective ratio before irradiation.

Using the parametrized curve of the results shown in fig. 2 (eq. 2) we estimated the light yield ratio expected on the hadron calorimeter for $\eta = 0$ and $\eta = 1.5$ after an integrated luminosity of $10^6 pb^{-1}$. Before recalibrating longitudinally each of the 4 cells the light reduction in the first tile (the worst case) is 6.2% for $\eta = 1.5$ and 4.8% for $\eta = 0$. Assuming that it is possible to know the longitudinal profile of the damage, each of the four longitudinal sectors can be calibrated. In this case the light ratio in the first tile deviates by 1.1% and 1.8% from the calibration constant in the first sector (mean of 3 first tiles) for $\eta = 0$ and for $\eta = 1.5$ respectively.

Table 3- Light output ratio of each individual fibre type measured at a distance of 130 cm from the PMT over the signal measured at a distance of 40 cm from the PMT. The values given are normalized to the respective ratio before irradiation. See text for details.

Fibre Type	Y11(100)M	Y11(200)M	Y11(200)	Y7(150)	Y7(150)N	BCF91A
Ratio	0.88	0.89	0.88	0.83	0.89	0.85

3. Effect of Radiation Damage on the Performance of the TILECAL hadron calorimeter in the Barrel region.

To evaluate the effect of the radiation on the performance of the calorimeter jets of 300 GeV have been generated using GEANT and FLUKA in the ATLAS configuration (Accordion Lar/Pb e.m. and TILECAL had. calorimeter), at $\eta = 0$. An adequate weight was given to each cell in order to reproduce the light ratio of each tile after $10^6 pb^{-1}$, either at $\eta = 0$ or $\eta = 1.5$. In the e.m. calorimeter no degradation due to radiation was considered. Fig. 4 shows the signal distribution for 300 GeV jets at $\eta = 1.5$. We observe that even at $\eta = 1.5$ and without longitudinal calibration the effect of radiation on the jet energy resolution is marginal, as well as in the total light reduction. In table 4 are given the values of the increase of the jet energy resolution and total light reduction both at $\eta = 0$ and $\eta = 1.5$.

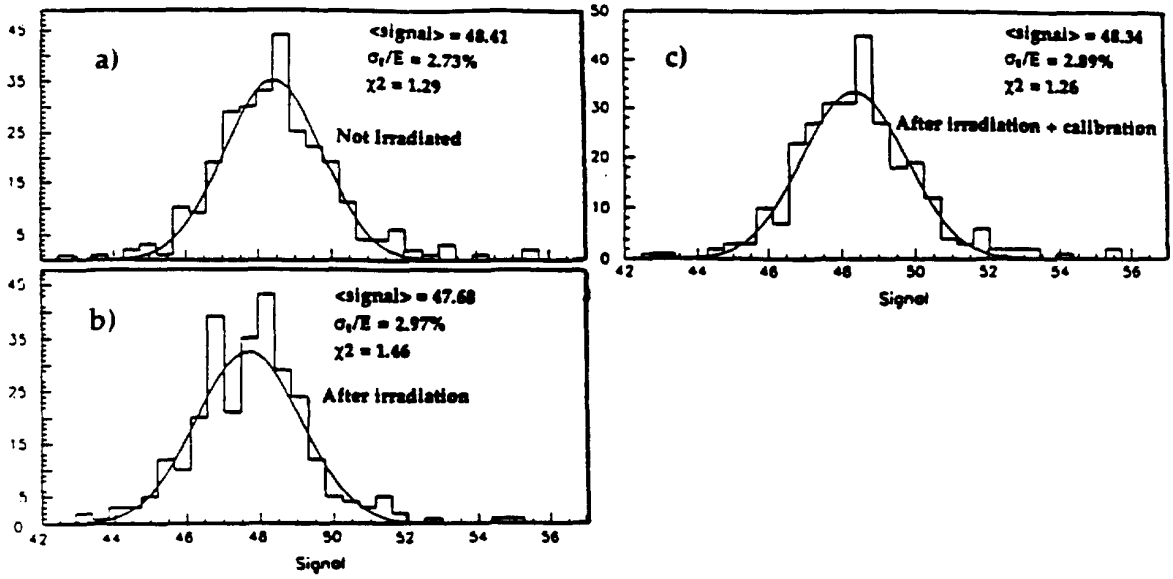

Fig. 4- The signal distribution for 300 GeV jets generated at $\eta = 1.5$ (a), after irradiation with the doses expected at $\eta = 1.5$ but without longitudinal calibration (b), after longitudinal calibration (c). It was considered the effect of irradiation after $10^6 pb^{-1}$.

Table 4- Expected degradation of the TILECAL hadron calorimeter performance in ATLAS for 300 GeV jets generated with GEANT and FLUKA. The values given are for an integrated luminosity of $10^6 pb^{-1}$.

	$\Delta(\sigma_{E/E})_{\eta=0}$ (%)	Δ Sig. $_{\eta=0}$ (%)	$\Delta(\sigma_{E/E})_{\eta=1.5}$ (%)	Δ Sig. $_{\eta=1.5}$ (%)
without calibration	+ 0.18	- 1.28	+ 0.24	- 1.51
after calibration	+ 0.10	- 0.10	+ 0.16	- 0.14

References:

1- A. Amorim, A. Henriques and A. Maio, Atlas Internal Note, CAL-NO-021, and ref. there in.

2- ATLAS Lettter of Intent, CERN/LHCC/92-4, LHCC/I2 (1992).

3- A. Ferrari et al., Atlas Internal Note, CAL-NO-005.

4- Johns K. at II International Conference On Calorimetry in High Energy Physics at TEXAS 1992.

5- Neutron cross section curves, Academic Press, Inc. Harcourt Brace Jovanovich, Publishers.

6-D. Green, FERMILAB Internal Note FERMILAB-FN-597.

8- SDC Technical Proposal, SDC-92-201, pag. 6-367.

9-A. Gomes et al., Radiat. Phys. Chem., Vol 41, No 1/2, pag. 185, 1993.

10- A. Byon-Wagner, ICFA Instrumentation Bulletin, No 9, pag. 23, April 1993.